Supplement of Biogeosciences, 18, 5831–5849, 2021
https://doi.org/10.5194/bg-18-5831-2021-supplement

Biogeosciences
Open Access

Supplement of

Fast local warming is the main driver of recent deoxygenation in the northern Arabian Sea

Zouhair Lachkar et al.

Correspondence to: Zouhair Lachkar (zouhair.lachkar@nyu.edu)

Oxygen equations in the model

The detailed description of the oxygen representation in the model is given in Lachkar et al. (2016). Below, we list the model equations that govern O_2 evolution. The conservation equation for oxygen O_2 in the model can be written as:

$$\frac{\partial O_2}{\partial t} = \mathcal{L}(O_2) + J_b O_2 + J_g O_2$$

where $\mathcal{L}$ is the 3-D transport operator, which represents advection and mixing; $J_b O_2$ and $J_g O_2$ are the source-minus-sink (SMS) terms for O_2 driven by biology and gas exchange, respectively.

The SMS term $J_b O_2$ is modeled as:

$$J_b O_2 = \overbrace{R_{O:N_{NO_3}} \times F_{NewP} + R_{O:N_{NH_4}} \times F_{RegP}}^{\text{sources}}$$
$$- \overbrace{2 \times F_{Nitrific} - R_{O:N_{NH_4}} \times \left(F_{Zmetab} + \mathcal{H}(O_2 - O_2^{den}) \cdot (F_{rs} + F_{rl}) + F_{rsed}\right)}^{\text{sinks}}$$

where $R_{O:N_{NO3}}$ and $R_{O:N_{NH4}}$ represent the O_2:N stoichiometric ratios for uptake of NO_3 and NH_4, respectively. F_{NewP} and F_{RegP} refer to new and regenerated production fluxes. F_{Nitrif} represents nitrification and F_{Zmetab} zooplankton basal metabolism. Finally, F_{rs} and F_{rl} are the remineralization fluxes of small and large detritus and F_{rsed} is the remineralization flux in the sediment layer. O_2^{den} is the oxygen threshold for denitrification and $\mathcal{H}(O_2 - O_2^{den})$ the Heaviside function defined as

$$\mathcal{H}(O_2 - O_2^{den}) = \begin{cases} 1, & \text{if } O_2 \geq O_2^{den} \\ 0, & \text{otherwise} \end{cases}$$

The parameter values and units for the stoichiometric ratios and the O_2 threshold for denitrification are given in Table 1.

The source-sink term $J_g O_2$ is added only as surface boundary condition and is modeled following the standard Ocean Carbon-Cycle Model Intercomparison Project (OCMIP-2) air-to-sea flux formulation:

$$J_g O_2 = K_w (O_2^{sat} - O_2^{surf}) / \Delta z$$

where Δz is the thickness of the surface layer, K_w is the O_2 gas transfer (piston) velocity, O_2^{surf} is the surface O_2 concentration, and O_2^{sat} is the O_2 saturation concentration at 1 atm total pressure, computed from temperature and salinity, based on Garcia and Gordon (1992). The piston velocity K_w is modeled following the standard OCMIP-2 formulation assuming a quadratic dependence on the wind speed Wanninkhof (1992), using the coefficient for long-term winds.

At suboxic O_2 concentrations ($O_2 < {O_2}^{den}$), nitrification ceases and the remineralization rate is reduced by 50%. Additionally, aerobic remineralization of small and large detritus is replaced by water column denitrification, where nitrate replaces oxygen as the electron acceptor. The conservation of nitrate in the model can be described by

$$\frac{\partial NO_3}{\partial t} = \mathcal{L}(NO_3) + F_{Nitrific} - F_{NewP} - F_{denit}$$

where $\mathcal{L}$ is the 3-D transport operator, and $F_{Nitrific}$ and F_{NewP} represent the source and sink terms of nitrate due to nitrification and new production, respectively. The denitrification flux F_{denit} is represented in the model as

$$F_{denit} = R_{N:C_{det}} \times R_{C:N_{Phy}} \times (F_{rs} + F_{rl})$$

where $R_{N:C_{det}}$ is the N:C ratio for denitrification and $R_{C:N_{Phy}}$ the C:N ratio for phytoplankton. Finally, benthic denitrification is represented in the model following the parameterization of Middelburg et al. Middelburg et al. (1996).

Analysis of model drift

In order to analyze the model drift, we show the AS domain-averaged salinity and O_2 in the top 200 m and between 200 and 1000 m in the climatological simulation and over the 4 cycles of interannual forcings (Fig S2 and Fig S3). In the top 200 m, the drift in salinity becomes very small already by the end of the climatological integration. During the interannual forcing integration, the average salinity over the 29 year period remains stable across the different integration cycles (Fig S2). Below 200m, the salinity drift decreases over time and becomes very limited by the end of the internannual forcing integration, with an average salinity drop between the 3rd and the 4th cycle of less than 0.001 psu (Fig S2). In the top 200 m, the AS domain-averaged O_2 initially drops rapidly but then slowly increases after the first 30 years of the climatological forcing integration. During the interannual forcing integration period, the oxygenation trend continues although at a weaker rate, with O_2 increasing by 1.2 mmol m^{-3} between the 1st and the 4th cycle (Fig S3). Below 200 m, O_2 increases initially at a relatively fast rate (15 mmol m^{-3} decade^{-1}), but this rate slows down by the end of the climatological forcing period to (0.6 mmol m^{-3} decade^{-1}) and a quasi-stabilization by the end of the interannual forcing integration (Fig S3). As a result of the model drift during the climatological integration, the OMZ volume initially expands over the first 30 years of integration but slowly and continually shrinks afterwards (Fig S4). During the interannual forcing period, the volume of the OMZ displays larger interannual variations but is relatively stable between the different integration cycles (Fig S4). Contrasting the local trends in both the top 200 m and between 200 m and 1000 m in the last 29 years of the climatological integration to those from the last interannual cycle (control hindcast run) reveals that the O_2 trends purely driven by model drift in the climatological run are positive in most regions, contrasting with the negative trends obtained in the interannual control simulation (Fig S5). This indicates that our deoxygenation rate estimates are rather conservative and can be larger when correcting with the potential model drift.

Evaluation of the simulated mean state and seasonal variability

The model reproduces well the observed distributions of sea surface temperature (SST) inferred from the Advanced Very High Resolution Radiometer (AVHRR) satellite data in both winter and summer seasons (Fig S6). In particular, the model captures the intense temperature gradients prevailing in both seasons across the AS. Indeed, the model reproduces the strong temperature contrasts between the AS and its marginal seas, i.e., the Gulf and the Red Sea as well as the upwelling-driven cold SST tongue that develops in the west AS during summer. Similarly, the distribution of the mean surface salinity is in good agreement with that from the WOA2018 climatology (Fig S6). The AS surface circulation is similarly well represented in the model in both summer and winter seasons (Fig S7). In particular, the model simulates well the reversal of the Somali Current between summer and winter seasons as well as the prominent features of the surface circulation system including the Southern Gyre, the Great Whirl and the Southwest Monsoon Current in summer and the Northeast Monsoon Current and South Equatorial Countercurrent in winter (Schott et al., 2009).

The model reproduces relatively well the observed surface distribution of nitrate in both seasons, despite a tendency towards slightly overestimating surface concentrations in the oligotrophic open ocean and underestimating them in the northern AS during summer (Fig S8). The large-scale nitrate distribution at depth is also well captured by the model despite some local biases (Fig S9). The model reproduces the observed high chlorophyll-a concentrations associated with the winter and summer blooms in the northern and western AS, respectively (Fig S8). Furthermore, summer high chlorophyll concentrations off the Indian west coast are also relatively well captured by the model. In contrast, the model tends to substantially overestimate chlorophyll levels off the Somali coast and in the western AS in general. This discrepancy may result from the fact that the model does not represent iron and silicic acid that may be contributing to limiting productivity in this region (Koné et al., 2009).

A more quantitative assessment of the model performance is shown using Taylor diagrams (Taylor, 2001) that summarize three important statistics: (i) the correlation coefficient between the model and the observations, (ii) the standard deviation in the model relative to the observations and (iii) the centered root mean square (RMS) with respect to observations (Fig S10). To this end, in-situ observations from the World Ocean Database 2018 (WOD2018) were binned temporally and spatially into a 0.5° x 0.5° seasonal climatology covering the AS region. No spatial interpolation was performed and the model and observations are contrasted at the observation points only. This analysis confirms the relatively good agreement between model and observations. More specifically, it shows that surface temperature and salinity, as well as upper (400 m) ocean nitrate and O_2 distributions generally all agree well with observations with correlations above 0.9 and comparable standard deviations, across all seasons (Fig S10). The model shows a weaker performance though in simulating surface chlorophyll with correlations ranging from 0.42 during winter months to 0.67 during the Fall season (Fig S10).

Table S1. Definitions, values and units for the O_2 model parameters.

Parameter definition	symbol	value	unit
O_2:N stoichiometric ratio for uptake of NO_3	$R_{O:N_{NO3}}$	9.375	mol-O_2 (mol-N)$^{-1}$
O_2:N stoichiometric ratio for uptake of NH_4	$R_{O:N_{NH4}}$	7.375	mol-O_2 (mol-N)$^{-1}$
C:N ratio for phytoplankton	$R_{C:N_{Phy}}$	6.625	mol-C (mol-N)$^{-1}$
N:C ratio for denitrification	$R_{N:C_{det}}$	0.8	mol-N (mol-C)$^{-1}$
O_2 threshold for denitrification	${O_2}^{den}$	4	mmol (m)$^{-3}$

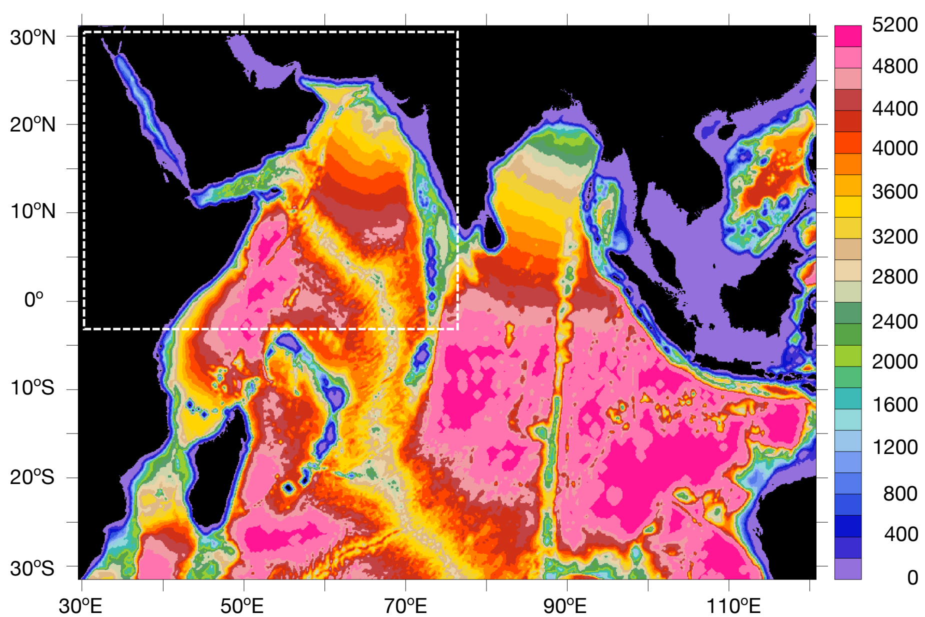

Figure S1. Model domain and seafloor bathymetry. The model domain covers the full Indian Ocean from 31°S to 31°N and 30°E to 120°E. The color shading shows the sea floor bathymetry (in m). The white dashed square highlights the region of interest used for the analysis and plots throughout the whole paper (3.5°S to 30°N and 32°E to 76°E).

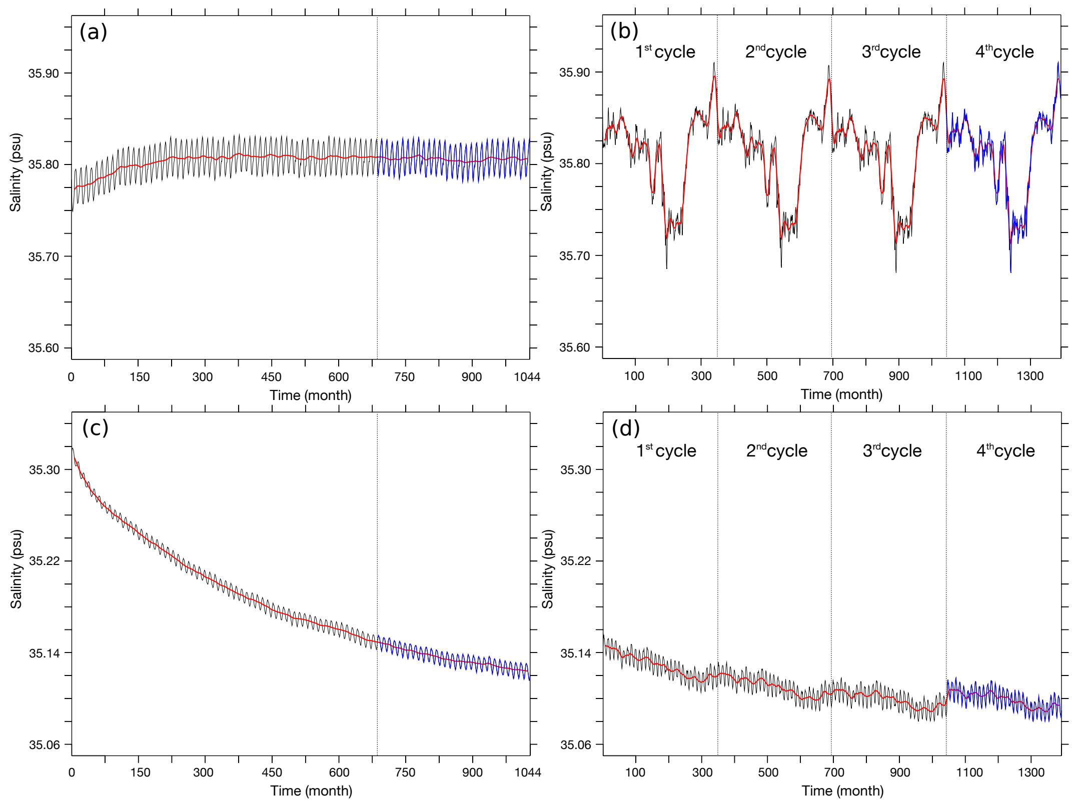

Figure S2. Model salinity drift. Arabian Sea averaged salinity in the top 200 m (a-b) and between 200m and 1000m (c-d) as simulated by the model as a function of time (black curve). The low-pass filtered data are shown in red. Left panels (a-c) show salinity as simulated under climatological forcing (climatological run) and right panels (b-d) indicate the evolution of salinity under repeated four cycles of ERA forcing. The last 29 years of the climatological run as well as the (29 year long) last cycle of the hindcast run are highlighted in blue.

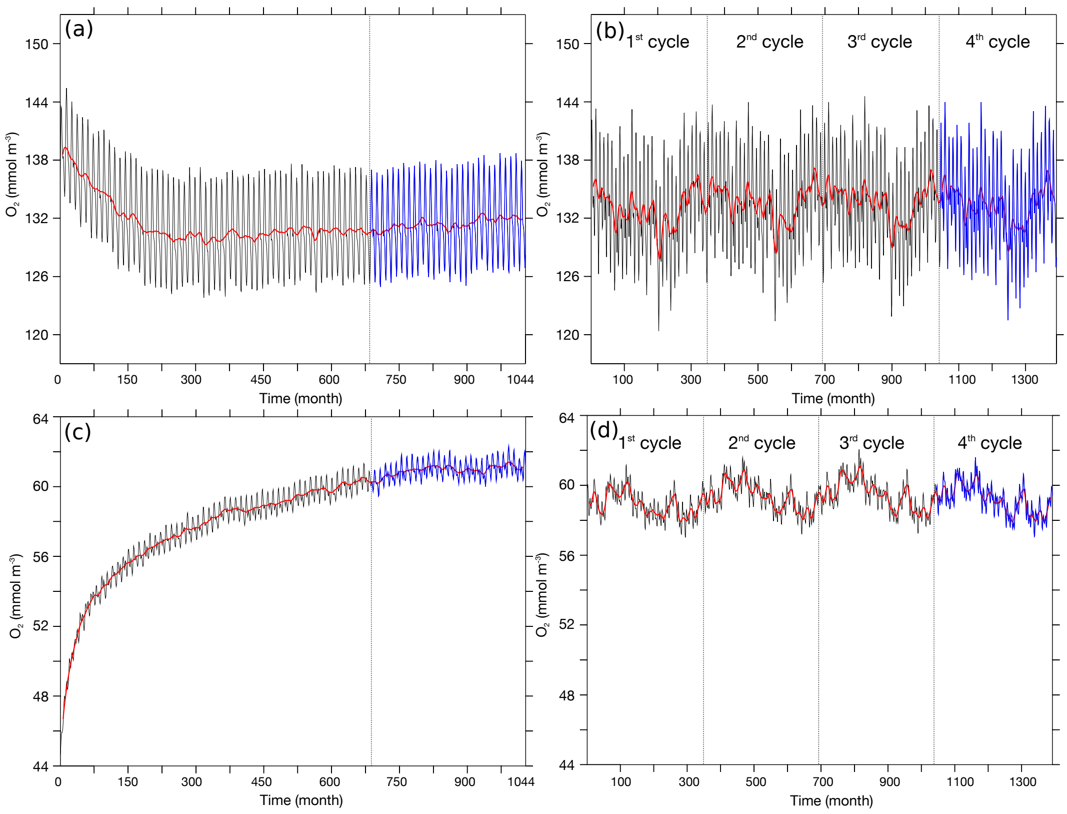

Figure S3. Model oxygen drift. Arabian Sea averaged oxygen in the top 200 m (a-b) and between 200m and 1000m (c-d) as simulated by the model as a function of time (black curve). The low-pass filtered data are shown in red. Left panels (a-c) show O_2 as simulated under climatological forcing (climatological run) and right panels (b-d) indicate the evolution of O_2 under repeated four cycles of ERA forcing. The last 29 years of the climatological run as well as the (29 year long) last cycle of the hindcast run are highlighted in blue.

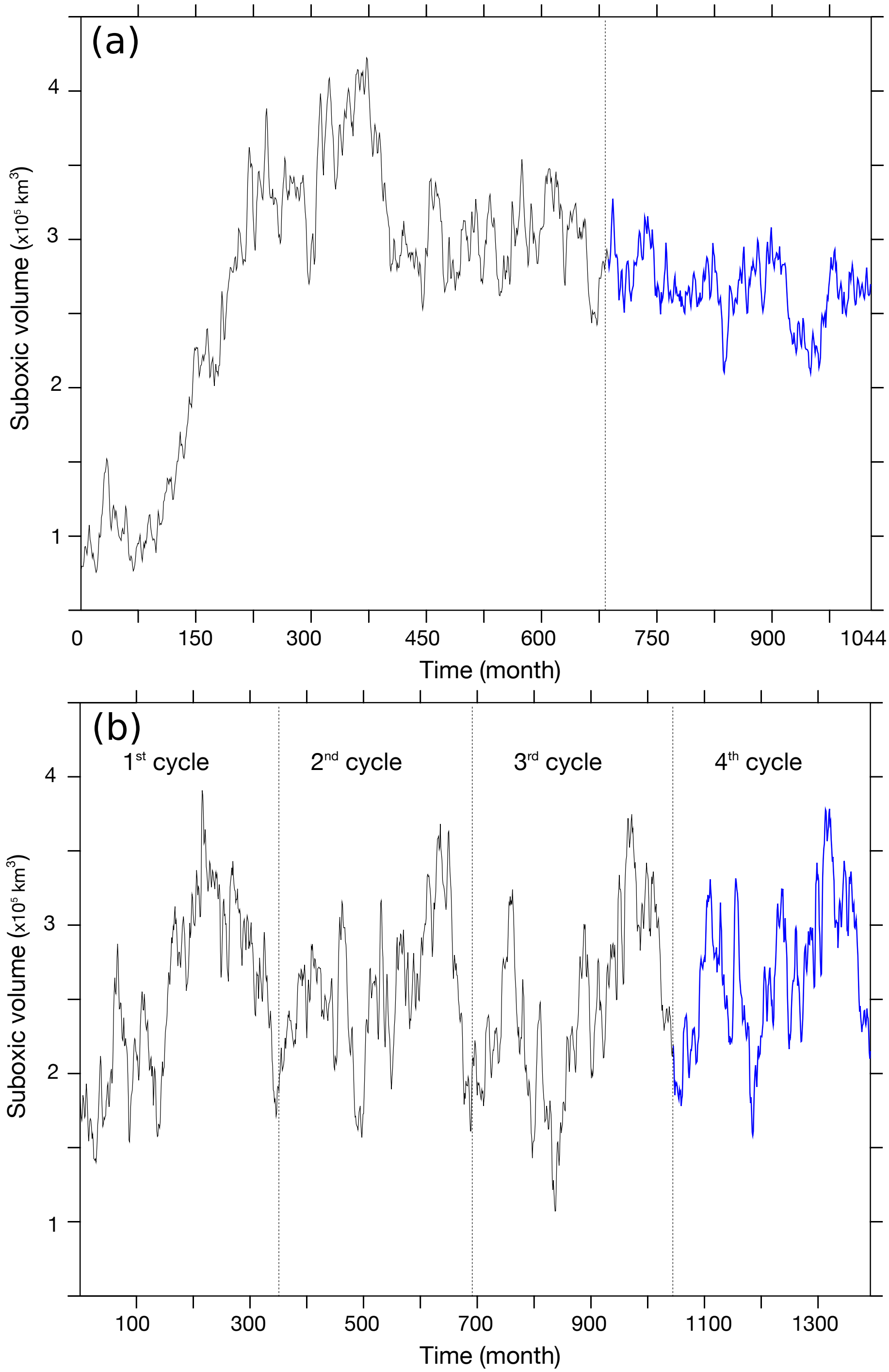

Figure S4. Model suboxic volume drift. Arabian Sea total suboxic volume as a function of time (black curve) as simulated by the model under (a) climatological forcing and (b) under repeated four cycles of interannual ERA forcing. The last 29 years of the climatological run as well as the (29 year long) last cycle of the hindcast run are highlighted in blue.

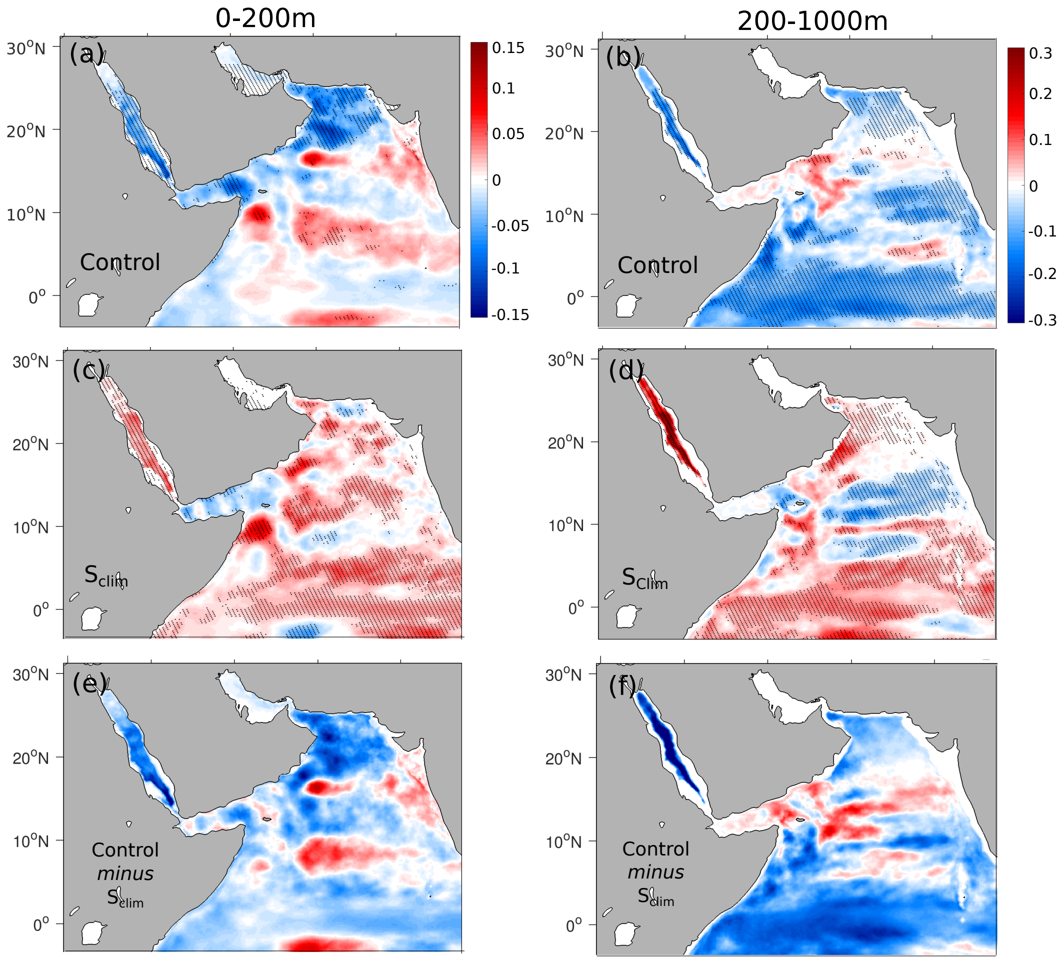

Figure S5. Deoxygenation rates in the hindcast simulation relative to the climatological run. Trends in O_2 inventories (in Gmol decade^{-1}) in (left) the top 200 m and (right) the 200-1000 m layer in the control hindcast simulation (top), the last 29 years of the climatological simulation (middle) and the difference between these trends (bottom). Statistically significant trends at 95% confidence interval following a Mann-Kendall (MK) test are represented by hatching.

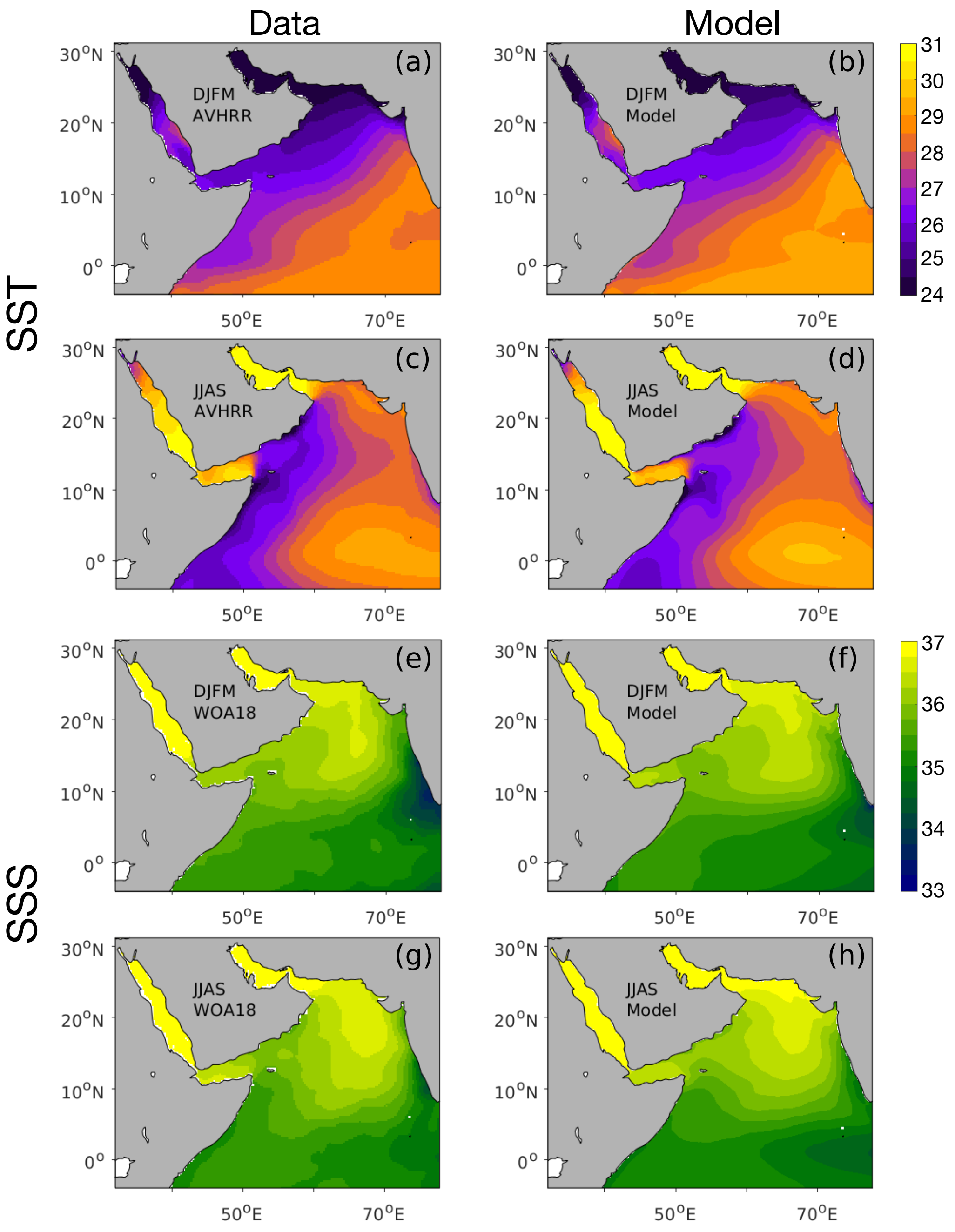

Figure S6. Evaluation of model simulated sea surface temperature and salinity (a-d) Sea surface temperature (in °C) as simulated in the model (right) and from the AVHRR satellite product (left) in winter (top) and summer (bottom) monsoon seasons.(e-h) Sea surface salinity (in PSU) as simulated in the model (right) and from the WOA-2018 dataset (left) in winter (top) and summer (bottom) monsoon seasons.

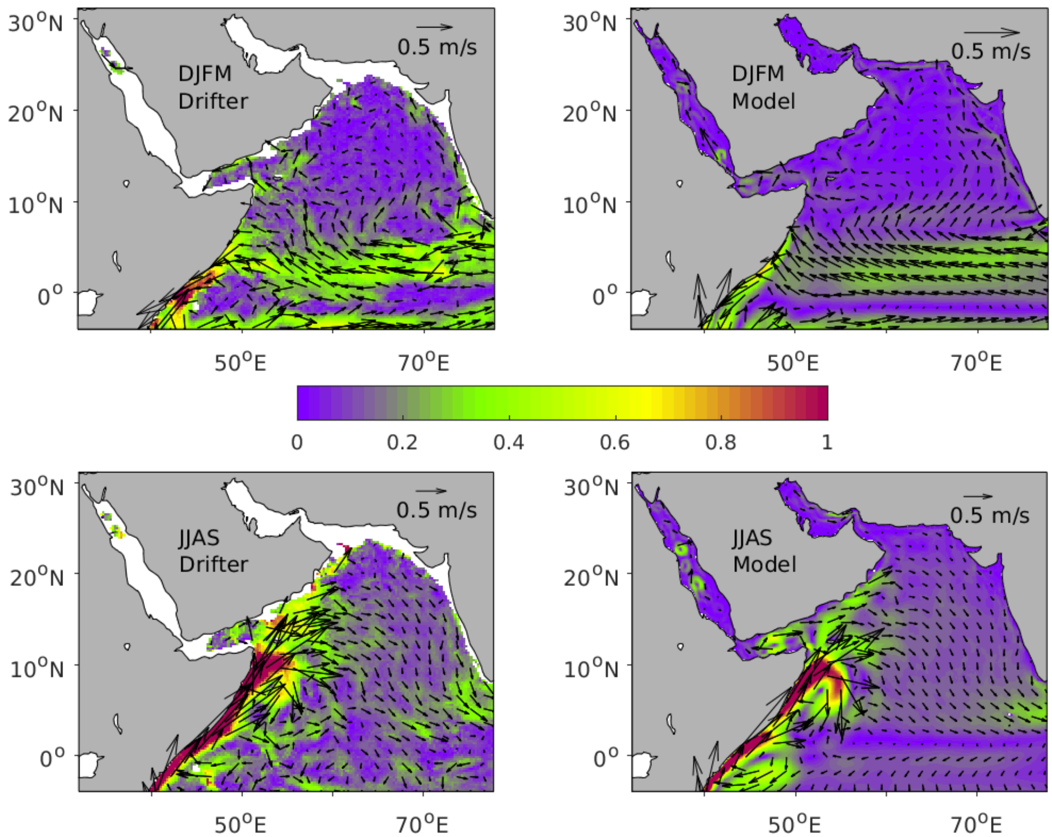

Figure S7. Evaluation of model simulated surface currents Surface currents (in $m\,s^{-1}$) as simulated in the model (right) and from surface drifter climatology of Laurindo et al. (2017) (left) during winter (top) and summer (bottom) monsoon seasons.

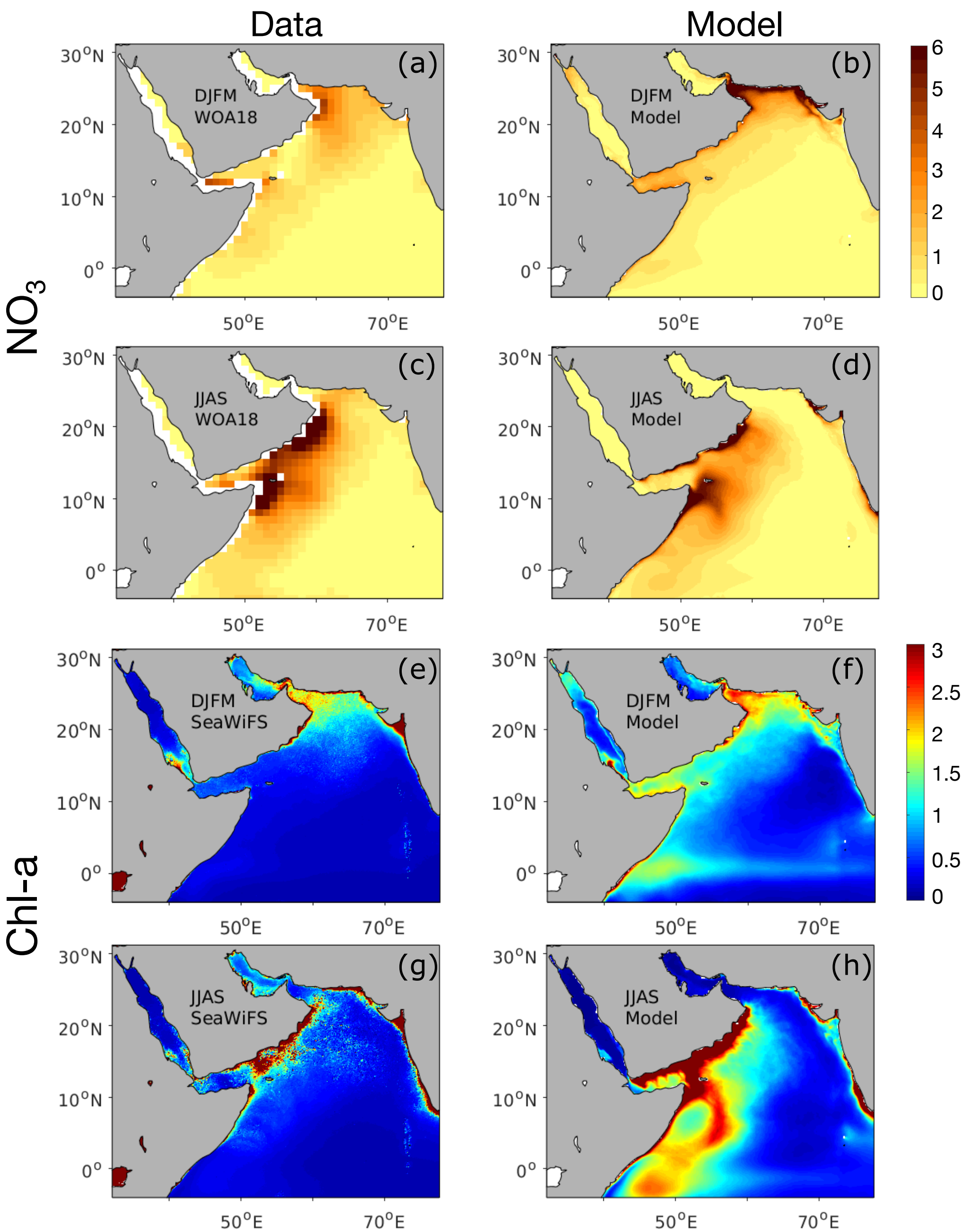

Figure S8. Evaluation of model simulated surface nitrate and chlorophyll-a (a-d) Surface NO_3^- (in mmol m^{-3}) as simulated in the model (right) and from the WOA-2018 dataset (left) in winter (top) and summer (bottom) monsoon seasons. (e-h) Sea surface chlorophyll-a concentrations (in mg m^{-3}) as simulated in the model (right) and from SeaWiFS climatology (left) during winter (top) and summer (bottom) monsoon seasons.

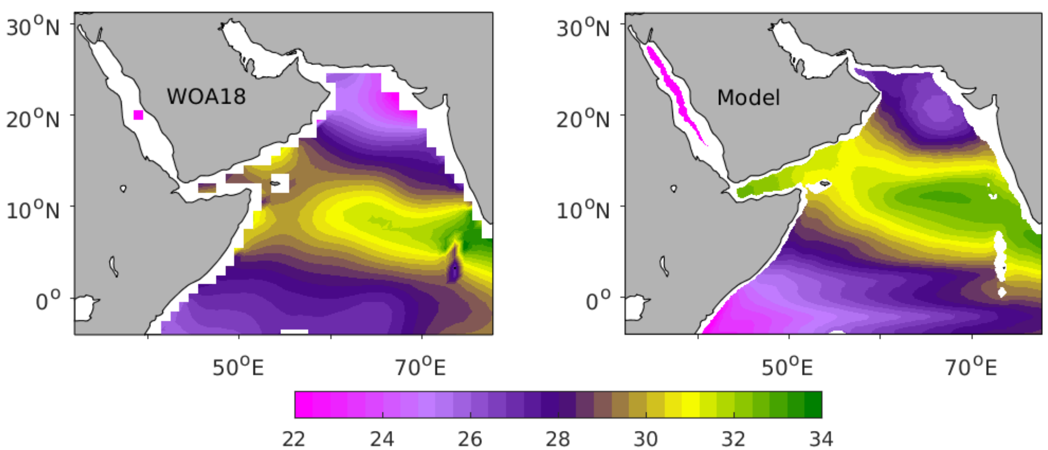

Figure S9. Evaluation of model simulated subsurface nitrate Annual mean NO_3^- averaged between 250 m and 700 m (in mmol m^{-3}) as simulated in the model (right) and from the WOA-2018 dataset (left).

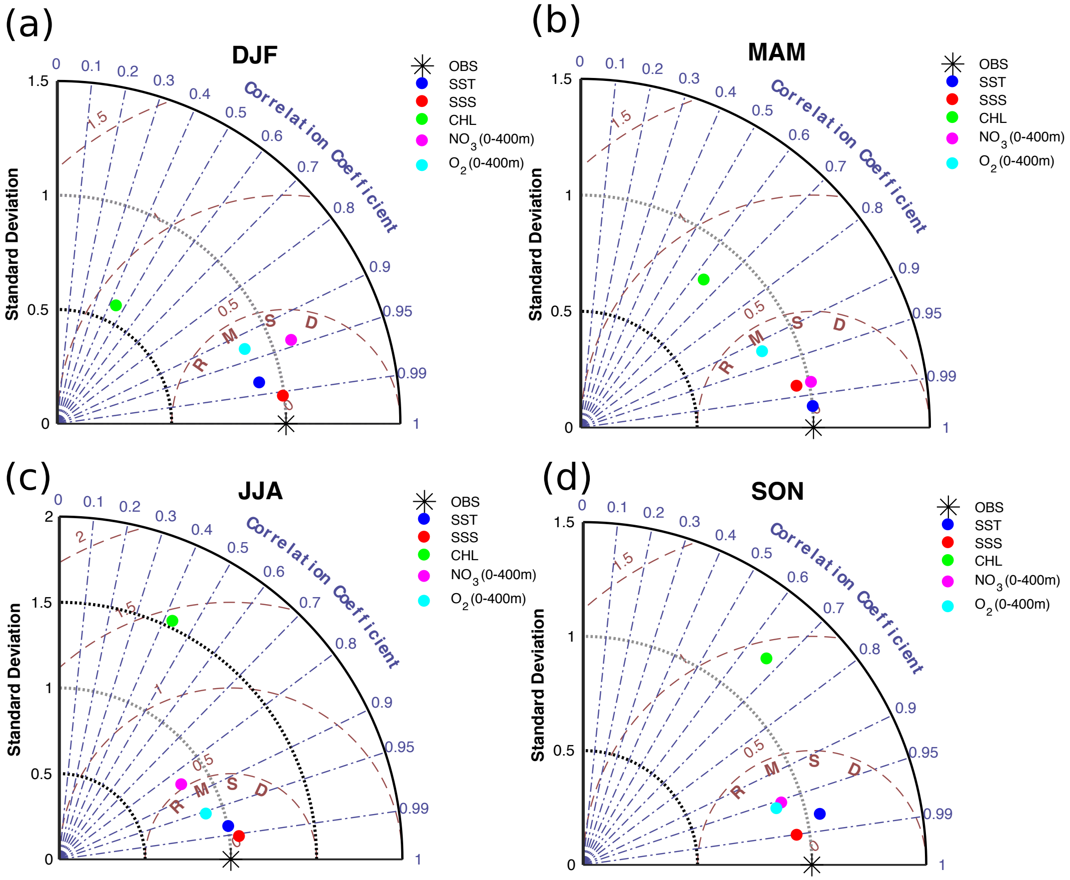

Figure S10. Model skill assessment with Taylor diagrams. Taylor diagram presenting statistical comparison of modeled and observed variables. Taylor (2001) diagram of sea surface temperature (blue), salinity (red), chlorophyll-a (green) and nitrate (purple) and oxygen (cyan) in the upper 400 m in (a) winter, (b) spring, (c) summer and (d) fall. The reference point in the Taylor diagram corresponds to observations. The radius (distance to the origin point) represents the modeled standard deviation relative to the standard deviation of the observations. The angle between the model point and the X-axis indicates the correlation coefficient between the model and the observations. Finally, the distance from the reference point to a given modeled field represents that field's centered root mean square (RMS) with respect to observations.

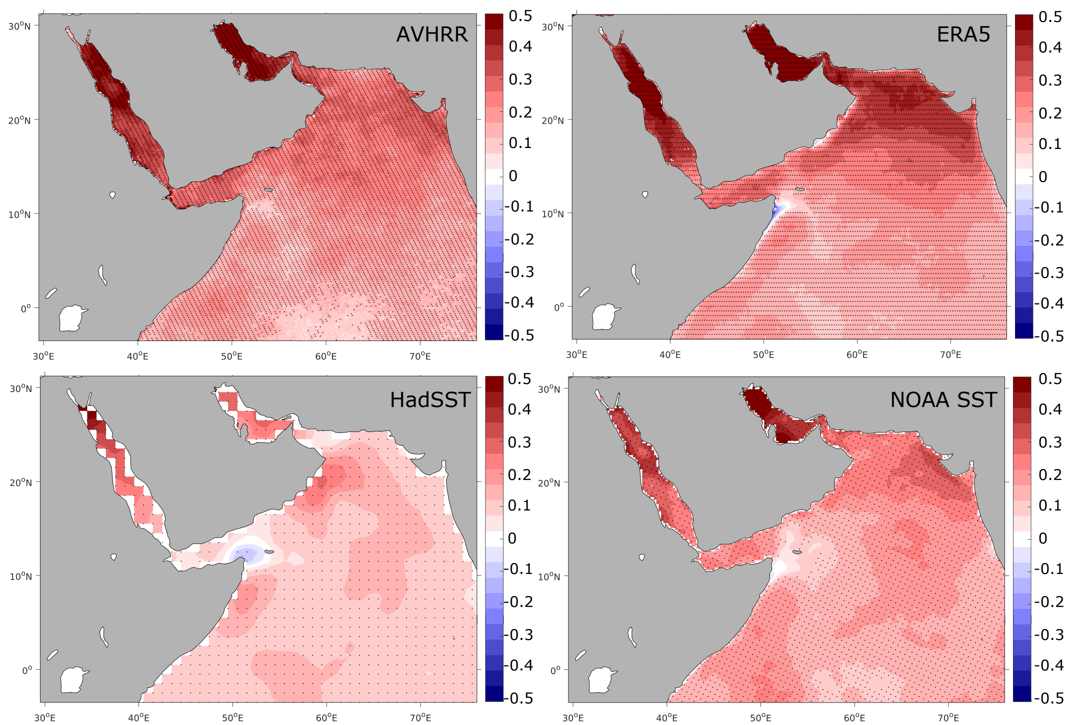

Figure S11. Comparison of trends in different SST products. Linear trends in sea surface temperature (in °C per decade) between 1982 and 2010 from AVHRR Pathfinder (top left), ERA5 (top right), Hadley Center SST (bottom left) and the NOAA OISST product (bottom right). Hatching represents statistically significant trends at 95% confidence interval following a Mann-Kendall (MK) test. The black rectangle in the top left figure indicates the location of northern Arabian Sea box

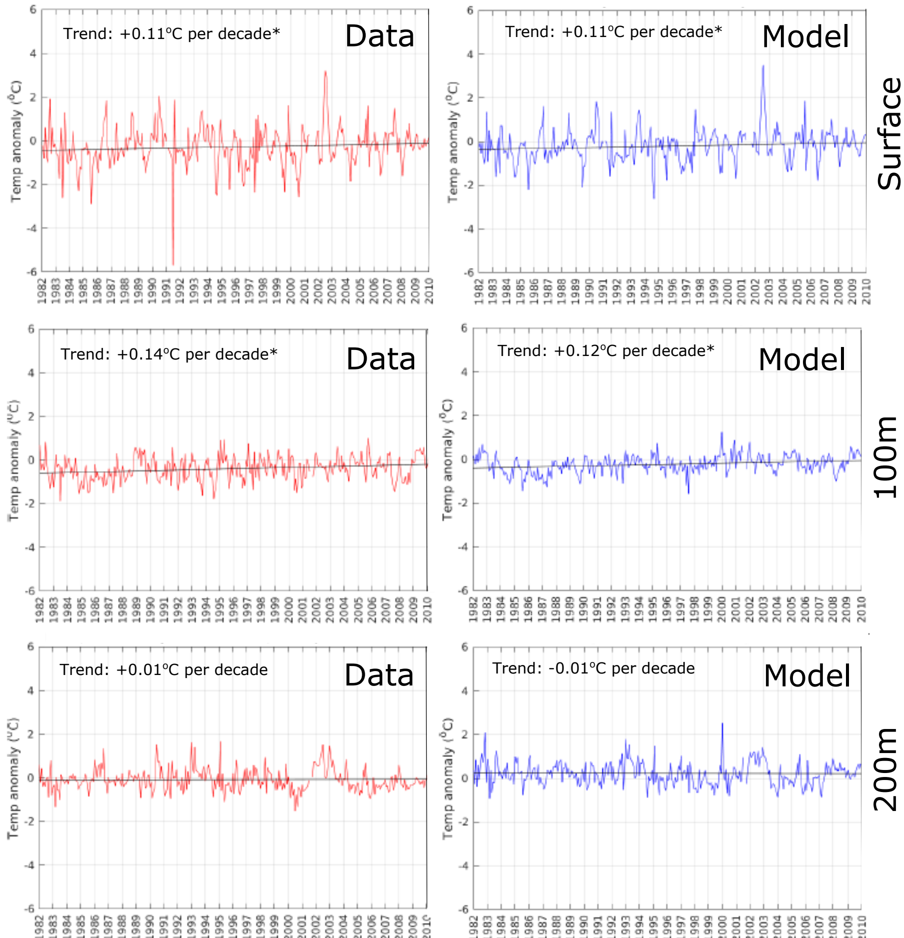

Figure S12. Evaluation of upper ocean warming. Interannual anomalies and linear trends in northern Arabian Sea temperature from WOD2018 observations (left) and ROMS model (right) at surface (top), 100m (middle) and 200m (bottom). Observed temperature interannual anomalies are estimated by binning in-situ observations in the northern AS box and deseasonalizing the time series. Model time series are evaluated similarly by subsampling the model outputs at observation points.

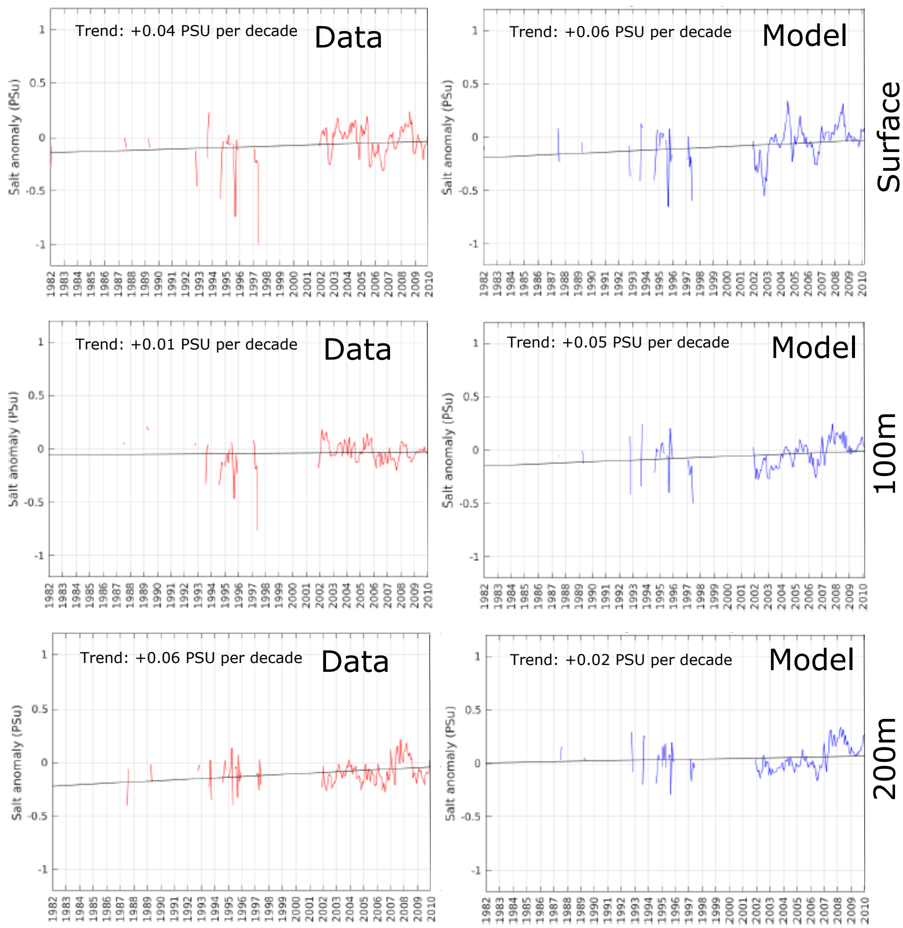

Figure S13. Evaluation of upper ocean salinity changes. Interannual anomalies and linear trends in northern Arabian Sea salinity from WOD2018 observations (left) and ROMS model (right) at surface (top), 100 m (middle) and 200 m (bottom). Observed salinity interannual anomalies are estimated by binning in-situ observations in the northern AS box and deseasonalizing the time series. Model time series are evaluated similarly by subsampling the model outputs at observation points.

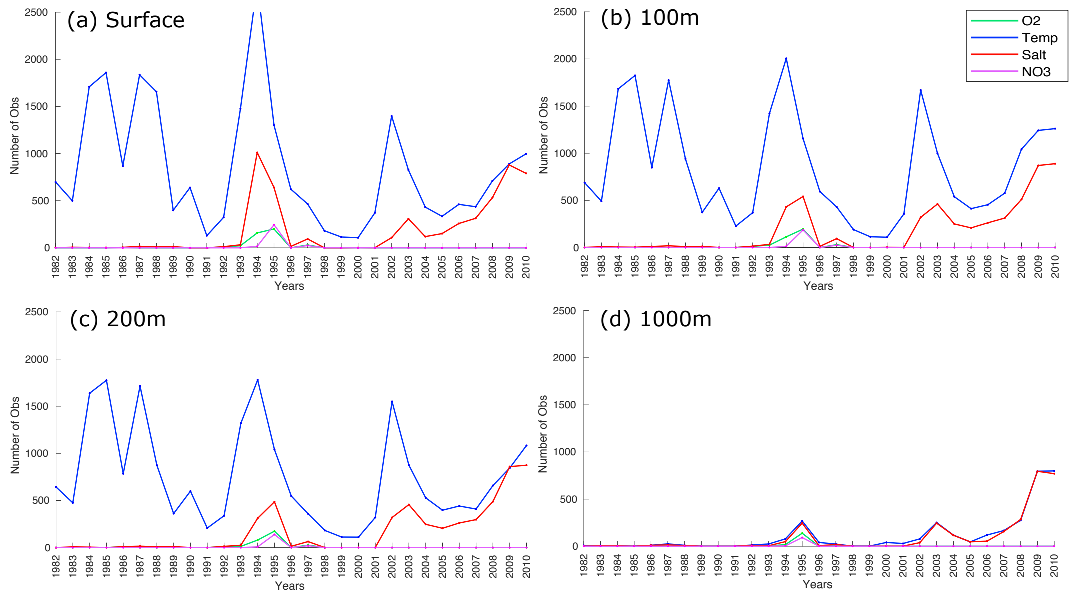

Figure S14. Temporal data coverage in the northern AS. Temporal data coverage over the study period for temperature (blue), salinity (red), O_2 (green) and NO_3 (purple). For each of the four variables, temporal data coverage is calculated by counting the number of annually binned observed data (WOD2018) in the northern AS box (shown in Figure 4a) at surface (top left), 100m (top right), 200 m (bottom left) and 1000 m (bottom right). The graphs indicate that temperature is the most well observed variable with a decent coverage that spans the study period, while NO_3, O_2 and to a lesser extent salinity show a much sparser coverage that precludes quantifying long-term trends over the simulated period.

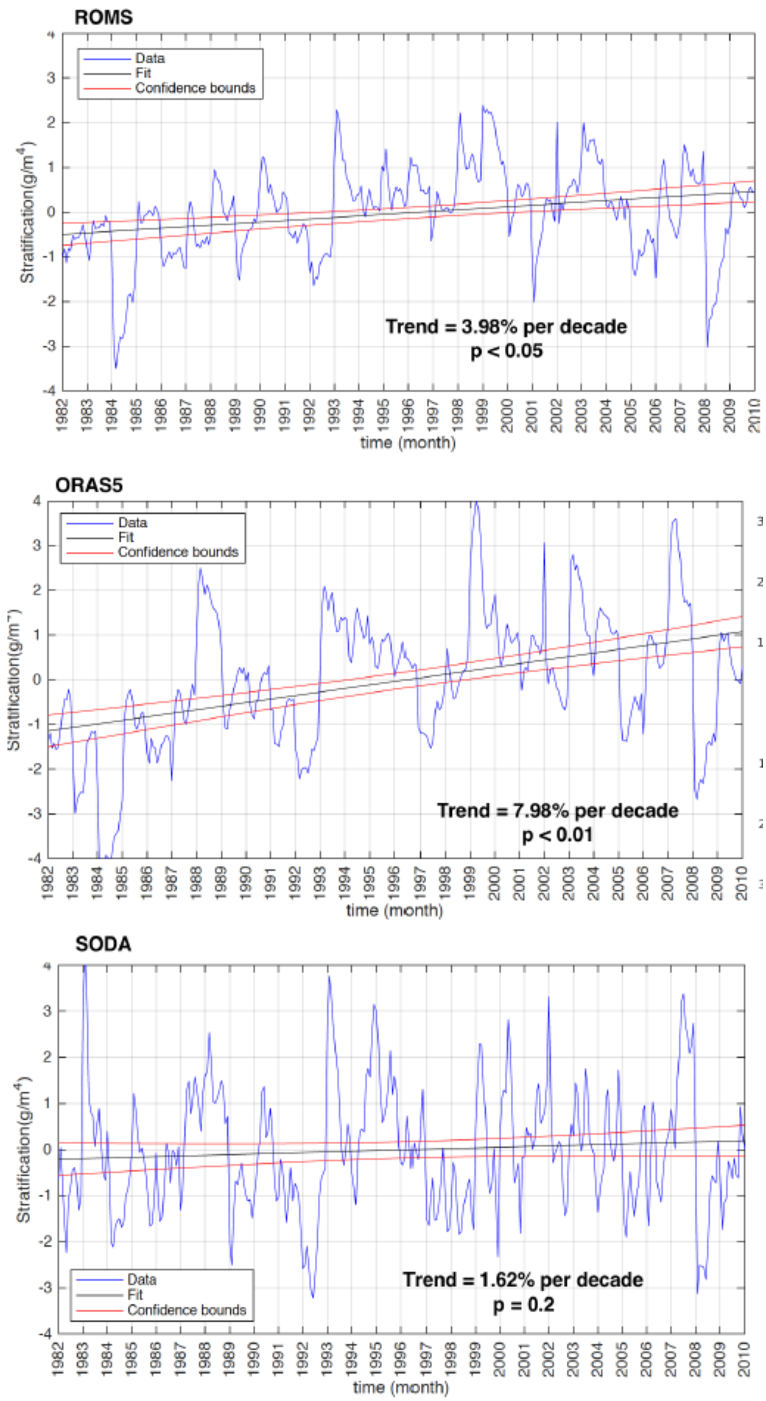

Figure S15. Evaluation of upper ocean stratification changes. Linear trends in vertical stratification at 100 m in the northern AS box (in g m^{-4} $decade^{-1}$) from the model (top), ORAS5 (middle) and SODA reanalyses (bottom).

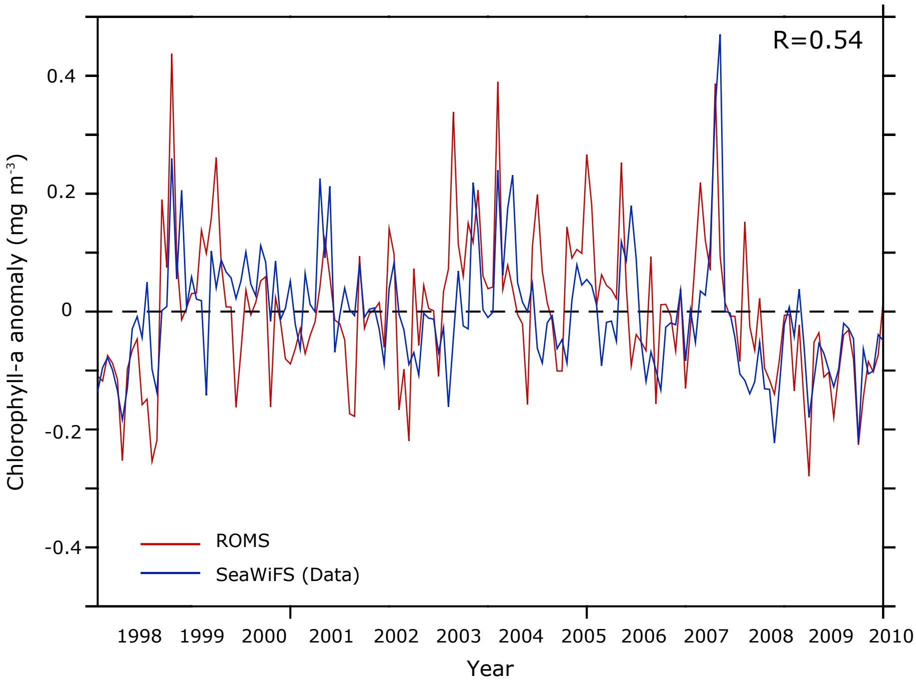

Figure S16. Evaluation of interannual variability in surface chlorophyll. Surface chlorophyll-a interannual anomalies averaged across the northern AS box as simulated in ROMS (red) and from SeaWiFS satellite data product (blue) over the common coverage period from 1997 to 2010. No significant trend can be identified over the period in either of the data or the model. Note the correlation (R=0.54) between modeled and observed interannual anomalies

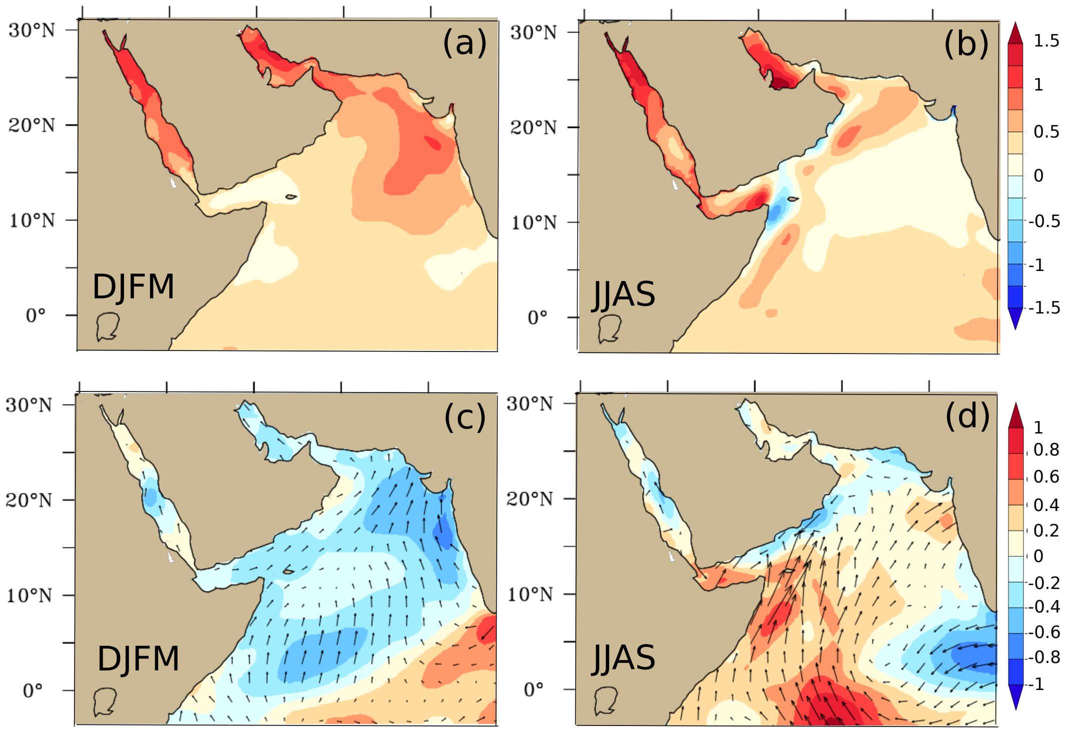

Figure S17. Long-term changes in atmospheric forcing. change in (left) winter and (right) summer (top) sea surface temperature (in °C) and (bottom) surface winds (color shading indicates changes in wind speed in $\mathrm{m\,s^{-1}}$ whereas arrows show changes in wind stress vector) between the first five years (1982-1986) and the last five years (2006-2010) of the study period.

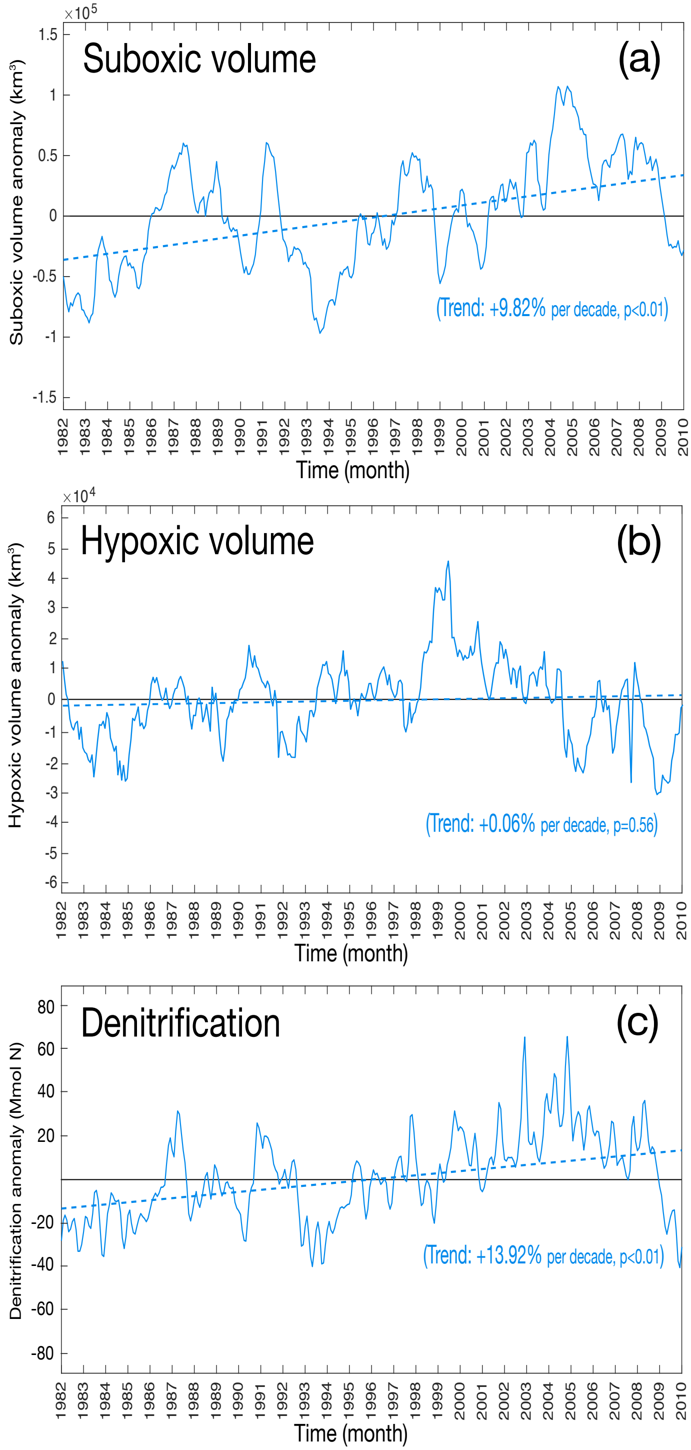

Figure S18. Changes in Arabian Sea Oxygen Minimum Zone intensity and denitrification. Interannual anomalies in the volume of (a) suboxia (b) hypoxia and (c) water column denitrification over the study period. The dashed lines indicate the trend lines.

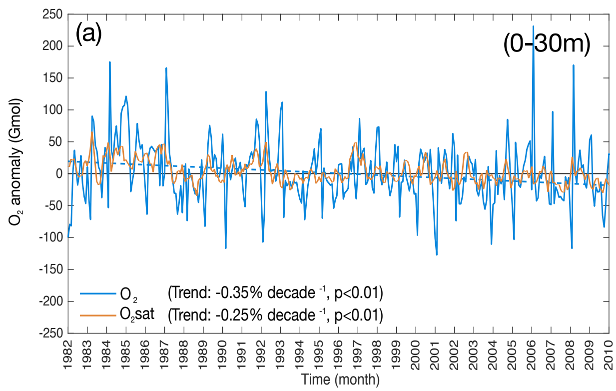

Figure S19. Drivers of northern AS surface deoxygenation. O_2 content (blue) and O_2 saturation (orange) anomalies in the top 30 m as a function of time. The blue dashed line indicates the trend line in O_2 inventory.

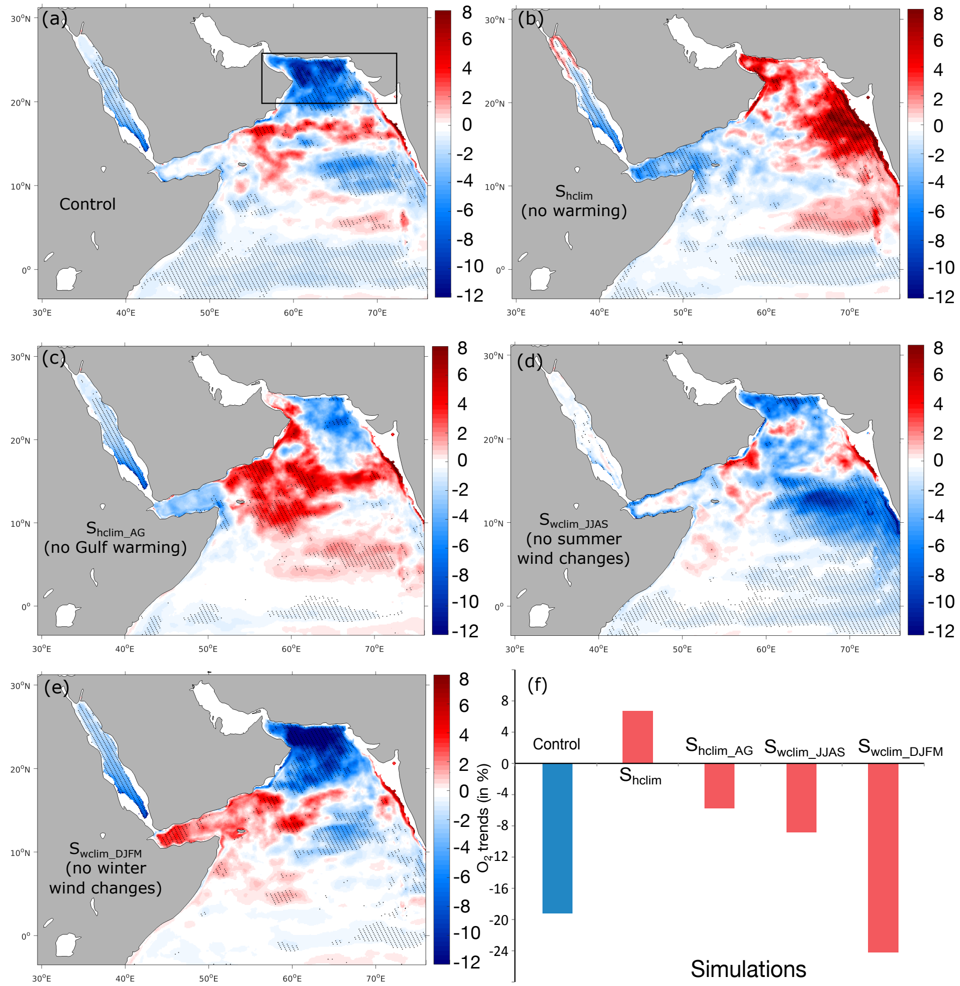

Figure S20. Deoxygenation rates under different atmospheric forcing scenarios. (a-e) Linear trends in O_2 inventories in the 100-1000 m layer (in % per decade) in the control (a), the S_{hclim} (i.e., no warming) (b), S_{hclim_AG} (i.e., no Gulf warming) (c), S_{wclim_JJAS} (i.e., no summer wind intensification) (d) and S_{wclim_DJFM} (i.e., no winter wind changes) (e) sensitivity simulations. (f) trends in O_2 inventory in the northern AS box in the control and different sensitivity simulations (in % of the mean O_2 inventory over the 1982-2010 period). Statistically significant trends at 95% confidence interval following a Mann-Kendall (MK) test are represented by hatching.

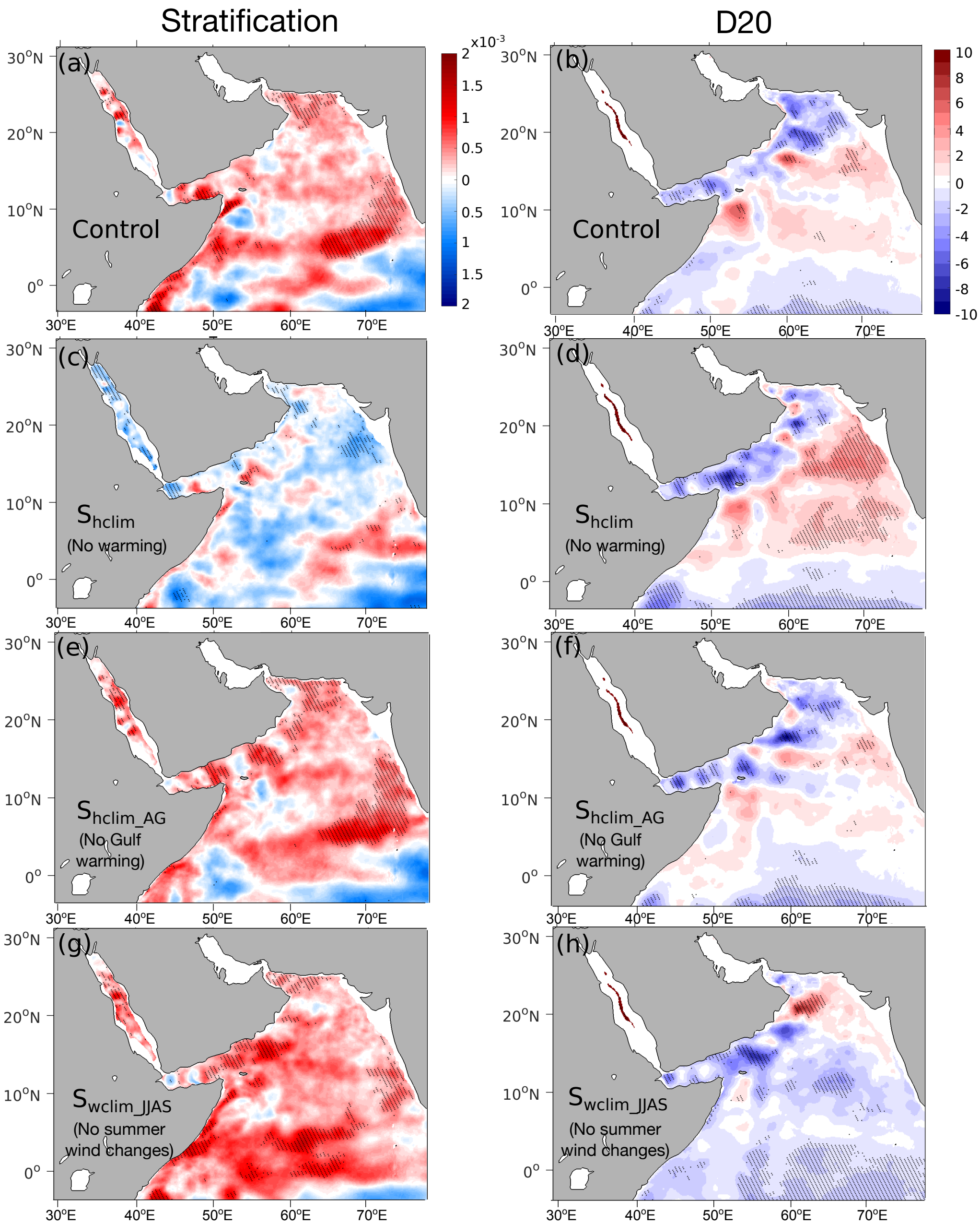

Figure S21. Vertical stratification and thermocline depth under different atmospheric forcing scenarios. Linear trends in (left) vertical stratification (in $\mathrm{g\,m^{-4}}$ decade^{-1}) and (right) depth of isotherm 20°C D20 (in m decade^{-1}) in the (a-b) control and (c-h) under different atmospheric forcing scenarios. Statistically significant trends at 95% confidence interval following a Mann-Kendall (MK) test are represented by hatching.

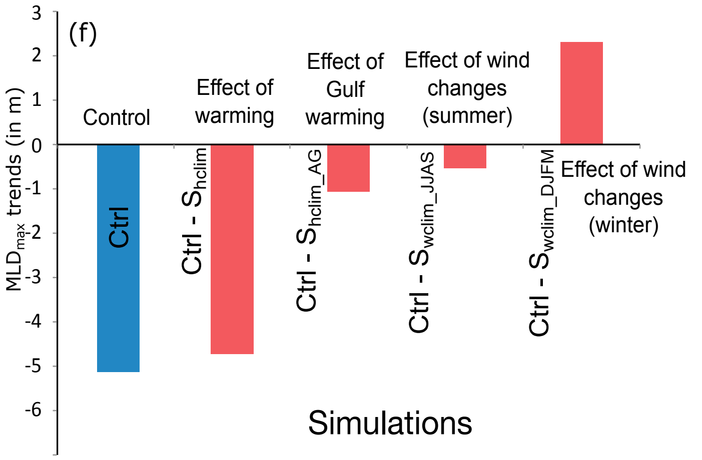

Figure S22. Effects of different atmospheric forcing perturbations on winter MLD. (a) Linear trends in winter MLD_{max} in the northern AS (in m) in the control run and differences between the control and the different sensitivity simulations.

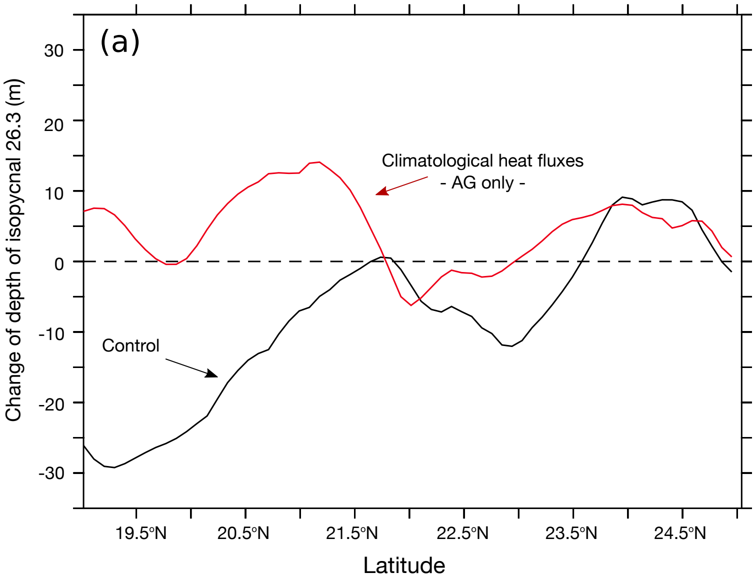

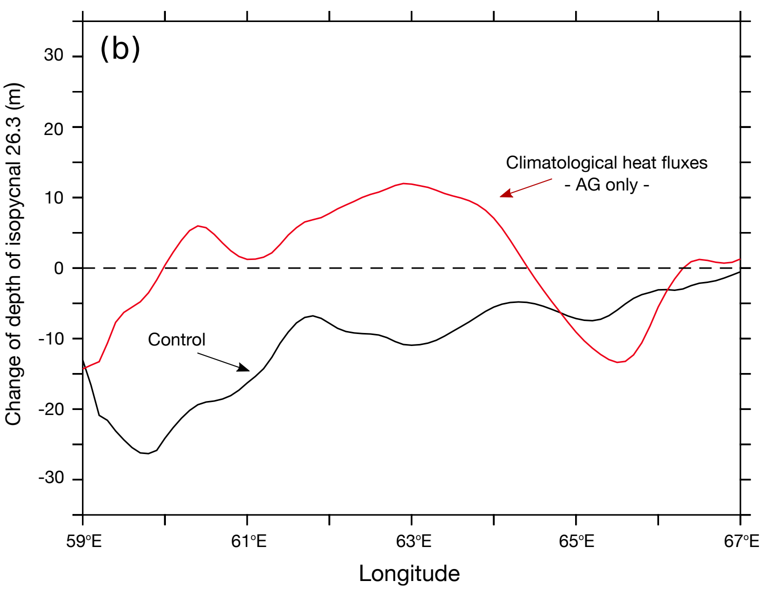

Figure S23. Depth of spreading of the Gulf waters. Change in the depth of isopycnal 26.3, corresponding to the Gulf water potential density, (in m) between the first five years (1982-1986) and the last five years (2006-2010) of the study period in the control (black) and in the S_{hclim_AG} (red) runs along (top) 60°E and (bottom) 20°N in the northern Arabian Sea.

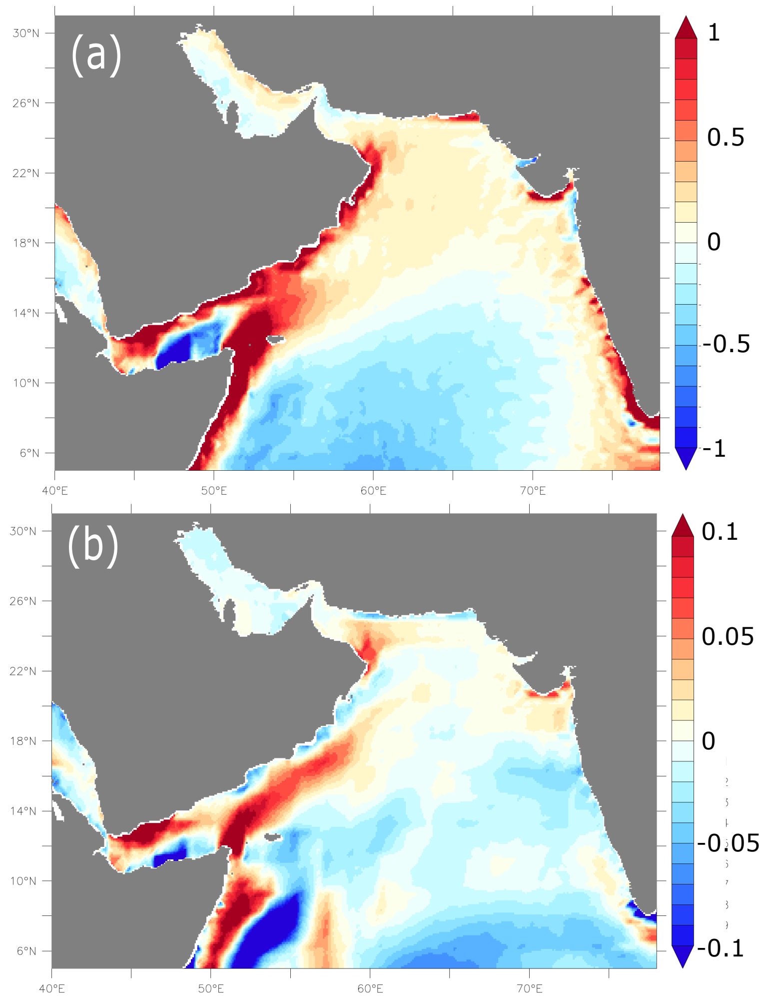

Figure S24. Average and trends in summertime Ekman pumping in the Arabian Sea. (a) Summer (JJAS) mean Ekman suction velocity (in m/day). (b) Linear trends in Ekman suction velocity during summer monsoon season (in m/day per decade). Positive values indicate upwelling (top) or an increase in upwelling (bottom).

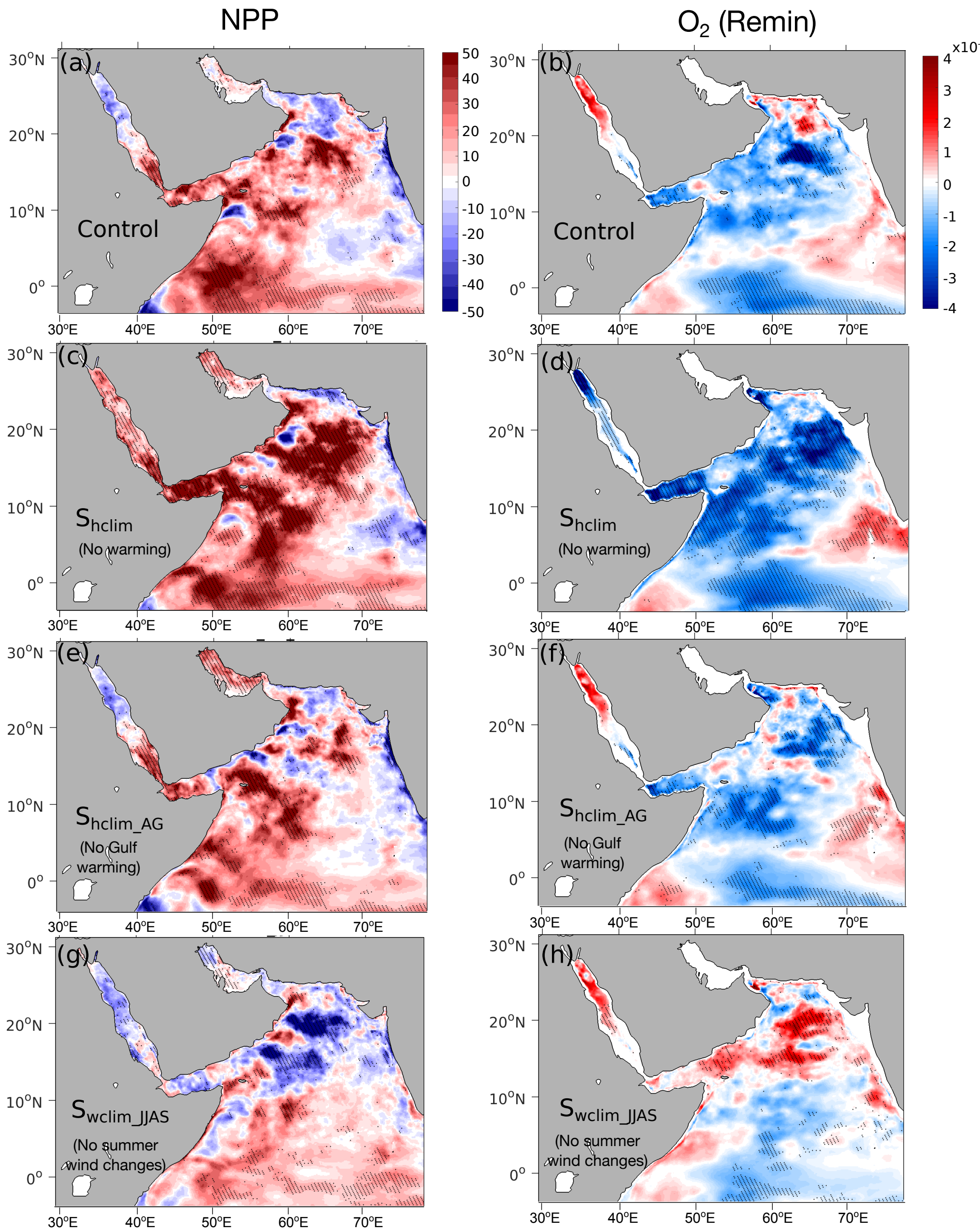

Figure S25. Net primary productivity and O_2 changes due to remineralization under different atmospheric forcing scenarios. Linear trends in (left) NPP (in mol m^{-2} yr^{-1} $decade^{-1}$) and (right) O_2 changes due to organic matter remineralization in the 200-1000 m layer (in mmol m^{-2} s^{-1} $decade^{-1}$) in the (a-b) control and (c-h) under different atmospheric forcing scenatios. Statistically significant trends at 95% confidence interval following a Mann-Kendall (MK) test are represented by hatching.

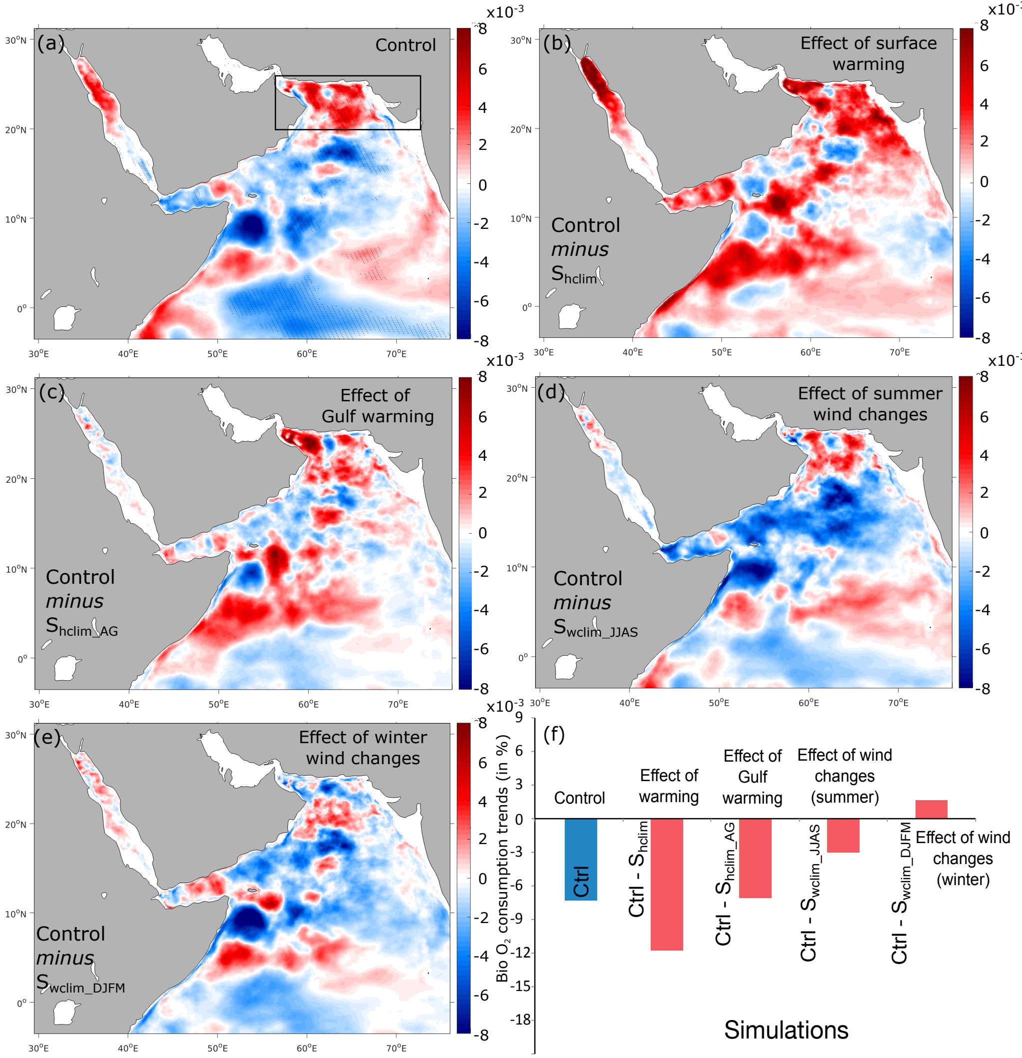

Figure S26. Effects of different atmospheric forcing perturbations on biological O_2 consumption. (a) Linear trends in biological O_2 consumption (in mmol m^{-2} s^{-1} decade^{-1}) in the control run (a positive trend indicates a weakening of O_2 consumption). (b-e) Difference in trends in biological O_2 consumption between the control run and the S_{hclim} (i.e., effect of warming), S_{hclim_AG} (i.e., effect of Gulf warming), S_{wclim_JJAS} (i.e., effect of summer wind intensification) and S_{wclim_DJFM} (i.e., effect of winter wind changes) sensitivity simulations (in mmol m^{-2} s^{-1} decade^{-1}). (f) Difference in biological O_2 consumption trends in the northern AS box between the control and the different sensitivity simulations (in % decade^{-1}).

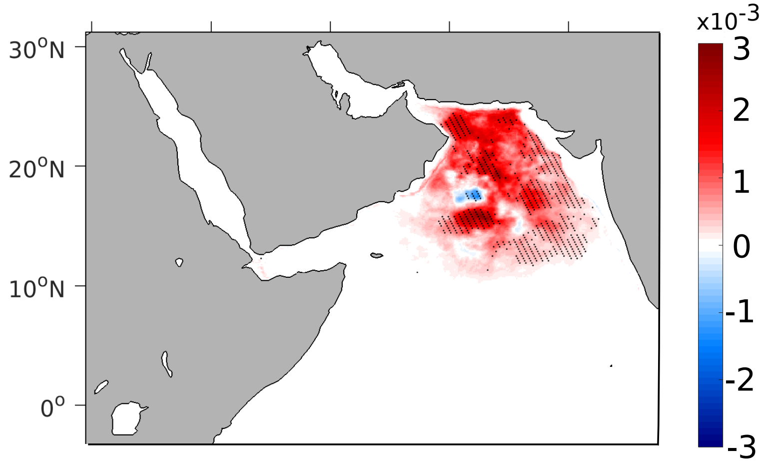

Figure S27. O_2 changes driven by denitrification Trends in O_2 between 200 and 1000 m (in mmol m^{-2} s^{-1} decade^{-1}) driven by change in denitrification.Statistically significant trends at 95% confidence interval following a Mann-Kendall (MK) test are represented by hatching.

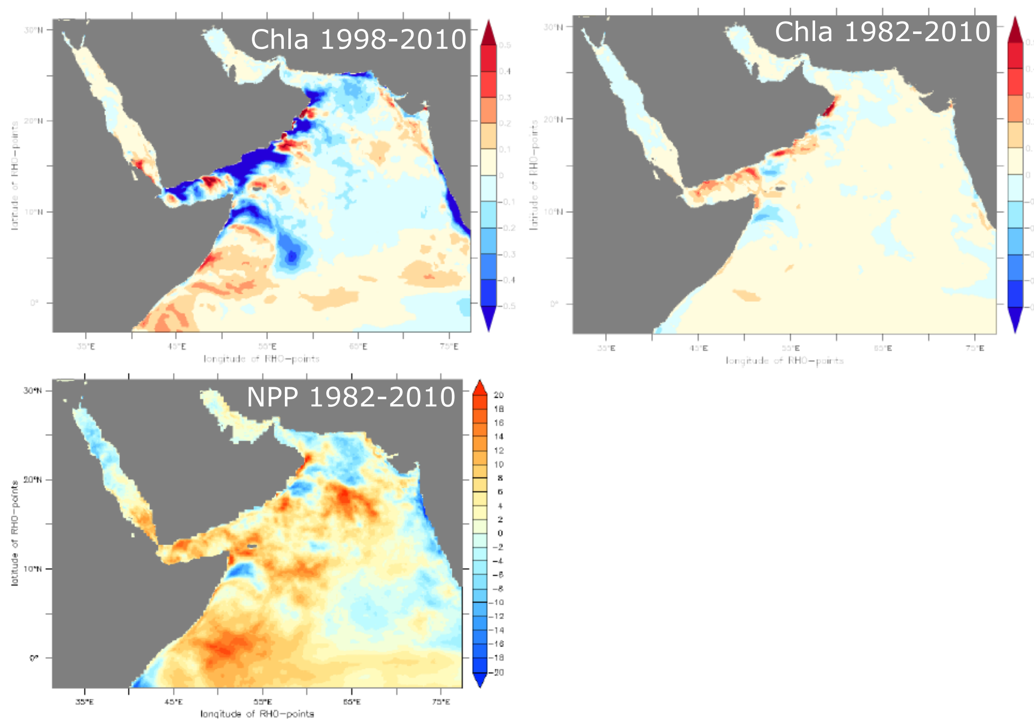

Figure S28. Trends in surface chlorophyll and NPP Linear trends in simulated surface chlorophyll (in mg/m3/decade) (top left) over the period (1998-2010) and (top right) between 1982 and 2010. (bottom left) linear trends in biological productivity between 1982 and 2010 (in mol/m2/yr/decade).

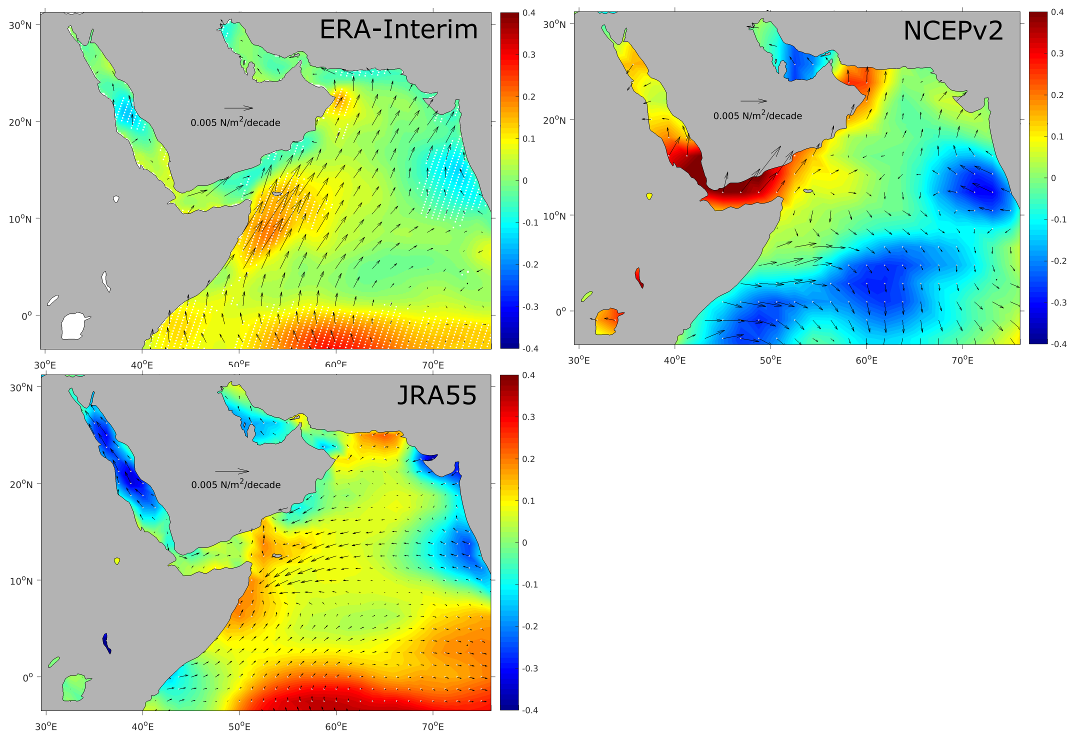

Figure S29. Surface wind trends in different reanalyses Linear trends in surface winds from ERA-Interim (top left, used to force the model), NCEPv2 (top right) and JRA55 (bottom left) reanalyses products. Color shading indicates trends in wind speed (in m s^{-1} decade^{-1}) whereas arrows show trends in wind stress vector.

References

Garcia, H. E. and Gordon, L. I.: Oxygen solubility in seawater: Better fitting equations, Limnology and oceanography, 37, 1307–1312, 1992.

Koné, V., Aumont, O., Lévy, M., and Resplandy, L.: Physical and biogeochemical controls of the phytoplankton seasonal cycle in the Indian Ocean: A modeling study, Indian Ocean Biogeochemical Processes and Ecological Variability, 185, 350, 2009.

Laurindo, L. C., Mariano, A. J., and Lumpkin, R.: An improved near-surface velocity climatology for the global ocean from drifter observations, Deep Sea Research Part I: Oceanographic Research Papers, 124, 73–92, 2017.

Middelburg, J. J., Soetaert, K., Herman, P. M., and Heip, C. H.: Denitrification in marine sediments: A model study, Global Biogeochemical Cycles, 10, 661–673, 1996.

Schott, F. A., Xie, S.-P., and McCreary Jr, J. P.: Indian Ocean circulation and climate variability, Reviews of Geophysics, 47, 2009.

Taylor, K. E.: Summarizing multiple aspects of model performance in a single diagram, Journal of Geophysical Research: Atmospheres, 106, 7183–7192, 2001.

Wanninkhof, R.: Relationship between wind speed and gas exchange over the ocean, Journal of Geophysical Research: Oceans, 97, 7373–7382, 1992.